JFM RAPIDS
journals.cambridge.org/rapids

Flapping dynamics of an inverted flag

**Daegyoum Kim†, Julia Cossé, Cecilia Huertas Cerdeira
and Morteza Gharib**

Division of Engineering and Applied Science, California Institute of Technology,
Pasadena, CA 91125, USA

The dynamics of an inverted flag are investigated experimentally in order to find the conditions under which self-excited flapping can occur. In contrast to a typical flag with a fixed leading edge and a free trailing edge, the inverted flag of our study has a free leading edge and a fixed trailing edge. The behaviour of the inverted flag can be classified into three regimes based on its non-dimensional bending stiffness scaled by flow velocity and flag length. Two quasi-steady regimes, straight mode and fully deflected mode, are observed, and a limit-cycle flapping mode with large amplitude appears between the two quasi-steady regimes. Bistable states are found in both straight to flapping mode transition and flapping to deflected mode transition. The effect of mass ratio, relative magnitude of flag inertia and fluid inertia, on the non-dimensional bending stiffness range for flapping is negligible, unlike the instability of the typical flag. Because of the unsteady fluid force, a flapping sheet can produce elastic strain energy several times larger than a sheet of the deformed mode, improving the conversion of fluid kinetic energy to elastic strain energy. According to the analysis of the leading-edge vortex formation process, the time scale of optimal vortex formation correlates with efficient conversion to elastic strain energy during bending.

Key words: aerodynamics, flow–structure interactions

1. Introduction

The interaction of an elastic sheet with a uniform free stream has been studied to understand flutter of a flag in wind, industrial processes for paper and thin films (Chang & Moretti 2002; Watanabe *et al.* 2002), and biological phenomena such as snoring and animal locomotion (Huang 1995; Zhang *et al.* 2000; Ristroph & Zhang 2008). In these studies, an elastic sheet had a fixed leading edge and a free trailing edge, a flag-type configuration. Many studies on the dynamics of the flag have focused on stability analysis (Guo & Païdoussis 2000; Tang, Yamamoto & Dowell 2003;

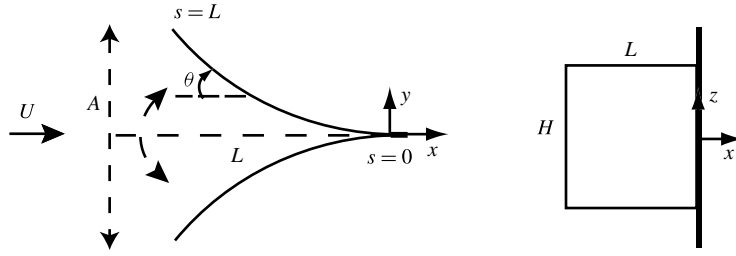† Email address for correspondence: daegyoum@caltech.edu

FIGURE 1. Schematic of an elastic sheet with a free front end and clamped rear end (top and side views). The dashed straight line is the initial shape of the sheet. A is the distance between two peaks of the tip in the y-direction, and s is the curvilinear coordinate from the rear end.

Argentina & Mahadevan 2005; Eloy *et al.* 2008) and the correlation between nonlinear dynamics and wake structure (Zhang *et al.* 2000; Connell & Yue 2007; Alben & Shelley 2008; Michelin, Smith & Glover 2008).

Recently, flow-induced flapping of an elastic sheet has been proposed as a new approach for harvesting fluid kinetic energy. This method requires fluid kinetic energy to be converted to strain energy of the structure. Then, the strain energy is converted to electrical energy with piezoelectric materials (Allen & Smits 2001; Taylor *et al.* 2001; Akaydin, Elvin & Andreopoulos 2010; Li, Yuan & Lipson 2011; Michelin & Doaré 2013). However, under the conditions previously studied, the critical flow velocity required for flapping is high, thereby making this an impractical method of energy harvesting. Thus, in most experimental studies, an upstream bluff body was used additionally to induce large oscillation of the downstream structure.

For the successful application of flow-induced oscillation to energy harvesting, the structure should be designed to easily become unstable at low critical flow velocity and have high excitation amplitude. In this regard, we study an alternative configuration to induce self-excited flapping of an elastic sheet. The configuration of our interest is an *inverted flag* in which the leading edge is free to move and the trailing edge is clamped (figure 1); the end conditions are the opposite of a typical flag. This design was motivated by the fact that a mechanical model with a free front end and a fixed rear end is generally more susceptible to instability to external axial loading than its counterpart with reverse end conditions. An inverted pendulum under gravitational force and a buckling bar under compressive force are such examples. The vibrating leaves of a tree also give a hint for this inverted flag design (Shao, Chen & Lin 2012). The leaves can flutter in a breeze regardless of their orientation to wind, which exemplifies that the flag-type configuration is not a necessary condition for flow-induced flapping.

To the best of our knowledge, little information is available on the coupling of an inverted flag configuration with a free-stream flow. Buchak, Eloy & Reis (2010) conducted an interesting study on the clapping behaviour of a stack of book papers clamped at a rear end. In their study, weight and elasticity of the papers were important factors in the oscillation of the papers against a free-stream flow. Guo & Païdoussis (2000) studied the linear stability with a potential flow model and claimed that an inverted elastic sheet was always unstable even in a vanishing free-stream speed with damping effects neglected, but no further information was provided on nonlinear dynamics. Here we experimentally investigate the flapping dynamics of an inverted elastic sheet in order to find how its stability is influenced by parameters

such as bending stiffness, flow velocity, fluid density, and sheet length. The effect of the parameters on drag and elastic strain energy is also examined. In addition, the flow structure developed by the sheet is identified, and its relationship with flapping dynamics and strain energy conversion is discussed.

2. Experimental setup

Experiments were conducted in an open-loop wind tunnel composed of an array of 10×10 computer fans (Johnson & Jacob 2009). The wind tunnel had a cross-section of 1.2 m $\times$ 1.2 m and was capable of producing free-stream velocity U between 2.2 and 8.5 m s^{-1}. The downstream edge of the sheet was clamped vertically between two long aluminium strips 2.5 cm wide and 1.3 cm thick (figure 1). The sheets were made from polycarbonate (Young's modulus $E = 2.38 \times 10^9$ N m^{-2}, Poisson's ratio $\nu = 0.38$, density $\rho_s = 1.2 \times 10^3$ kg m^{-3}), with thickness h of 0.8 mm. The height of the sheet H was fixed at 30 cm, and the lengths of the sheet L were 23, 27, and 30 cm, providing aspect ratios H/L between 1.0 and 1.3. The deformation of the sheet occurs primarily in the xy-plane, and sagging and twisting of the sheet due to gravitation were not observed; the deformation was two-dimensional. A small tip deflection $0.02 < \Delta/L < 0.04$ was found in the initial sheet configuration due to material defects.

For the observation of sheet motion, a white plastic tape was attached along the top edge of the sheet, and it was captured by a high-speed camera (Nanosense MK3, Dantec Dynamics) mounted over the top of the test section. For each sheet, images were recorded at 100 frames per second as the wind speed increased from 2.2 to 8.5 m s^{-1}. The top edge in the images was detected with a MATLAB script (Mathworks, Inc.). Aerodynamic drag D acting on the sheet was measured with two load cells (MB5, Interface, Inc.) connected to the top and bottom of the test section. The drag was also measured with only the clamping vertical strips and was subtracted from the total drag in order to obtain the net drag on the sheet.

Two non-dimensional dynamical parameters are important for the study of interaction between a fluid flow and an elastic sheet. These are non-dimensional bending stiffness β and mass ratio μ defined as follows (Connell & Yue 2007; Alben & Shelley 2008; Michelin *et al.* 2008):

$$\beta = \frac{B}{\rho_f U^2 L^3} \quad \text{and} \quad \mu = \frac{\rho_s h}{\rho_f L}, \tag{2.1}$$

where B is the flexural rigidity of the sheet ($B = Eh^3/12(1 - \nu^2)$), ρ_f is fluid density, and ρ_s is sheet density. Parameter β characterizes the relative magnitude of the bending force to the fluid inertial force, and μ describes the relative magnitude of solid to fluid inertial forces. In the wind tunnel experiments, β ranged from 0.04 to 1.50, and μ ranged from 2.5 to 3.3.

In order to investigate the effect of mass ratio on flapping dynamics, experiments were also conducted in water for low mass ratio of $O(10^{-3})$. The sheets were clamped vertically in a free-surface water tunnel with a test section 1.0 m wide and 0.5 m high. The water velocity ranged between 0.15 and 0.53 m s^{-1}. The lengths of the polycarbonate sheet 0.8 mm thick were 15 cm, 19 cm, and 23 cm. While β ranged from 0.05 to 1.38, μ was several orders of magnitude lower than that of the wind tunnel experiments, ranging from 0.004 to 0.006. A camera (IGV-B1920, Imperx, Inc.) was mounted below the floor of the test section, and the images of the bottom edge of the sheet were recorded at 10 frames per second as the water speed increases.

In addition to capturing images of the sheet, planar digital particle image velocimetry was performed in the water tunnel to visualize vortical structures of the flapping sheet. The tunnel was seeded with silver-coated hollow ceramic spheres of diameter 70 μm (AG-SL150-16-TRD, Potters Industries). The particles were illuminated by an Nd:YAG laser sheet (Gemini PIV, New Wave) at the middle height of the sheet. Image pairs were captured at a rate of 15 pairs per second, and processed with PIVview (PIVTEC GmbH). Each pair of images was cross-correlated with a multi-grid interrogation scheme. The first interrogation window size was 128×128 pixels with a 50 % overlap, and the final window size was 32×32 pixels with a 50 % overlap, which produces 119×66 grids with the size of 5.8 mm.

3. Results and discussion

3.1. *Three dynamical regimes*

First, the amplitude and flapping frequency of the elastic sheets are presented for high mass ratio of $O(1)$. The responses of the sheet can be divided largely into three modes, depending on non-dimensional bending stiffness β (figure 2). For β higher than 0.3, the sheet remains straight (straight mode, figure 2*c* i). For β lower than 0.1, the sheet bends in one direction and maintains a highly curved shape (deflected mode, figure 2*c* iv). Even though the sheet flutters slightly in both straight mode and deflected mode, the peak-to-peak amplitude of the tip A/L is less than 0.2 in these two modes, and flutter periodicity is not clear. Between these two quasi-static modes $(0.1 < \beta < 0.3)$, the sheet flaps from side to side, and the deflection of the sheet is periodic with nearly constant A/L (limit-cycle flapping mode, figures 2*c* ii, *c* iii and 2*d*). A/L increases drastically in the flapping mode, and plateaus to a range between 1.7 and 1.8. For $0.1 < \beta < 0.2$, the sheet continues to bend past where the tip is at maximum $|y|$, which results in slight decrease in the $|y|$-position of the tip at maximum deformation as described in figures 2(*c* iii) and 2(*d*). Within the flapping regime, the Strouhal number $f A/U$ does not show a plateau, unlike A/L, but has a maximum value of 0.14 around $\beta = 0.2$ (figure 2*b*).

The inverted flag shows several characteristics distinct from those of the typical flag with a clamped or pinned leading edge and a free trailing edge (e.g. Zhang *et al.* 2000; Connell & Yue 2007; Alben & Shelley 2008; Michelin *et al.* 2008). The inverted flag exhibits larger peak-to-peak amplitude, up to $A/L = 1.7$–1.8, than the typical flag. The large amplitude is realized because the aerodynamic force on the sheet, either lift or drag, always functions to destabilize the sheet and induce its deformation. In addition, the critical non-dimensional bending stiffness to initiate large-amplitude flapping from a straight mode is larger than the critical bending stiffness of the typical flag. The sheet used in this study was not self-excited when the end conditions of the edges were reversed to the conventional flag configuration. Moreover, while the typical flag exhibits periodic or chaotic flapping motion beyond a single critical bending stiffness, the inverted flag experiences large-amplitude oscillation only within a specific range of the bending stiffness. This trend of the oscillation within a limited range of the bending stiffness is somewhat analogous to the amplitude response of an elastically mounted cylinder in vortex-induced vibration (Shiels, Leonard & Roshko 2001). On the other hand, an inverted flag with very small bending stiffness beyond the bending stiffness range studied here may behave differently. A very flexible sheet could bend 180° around the clamped trailing edge and be parallel to the free stream, which results in the configuration similar to the typical flag. In this case, since the curl at the
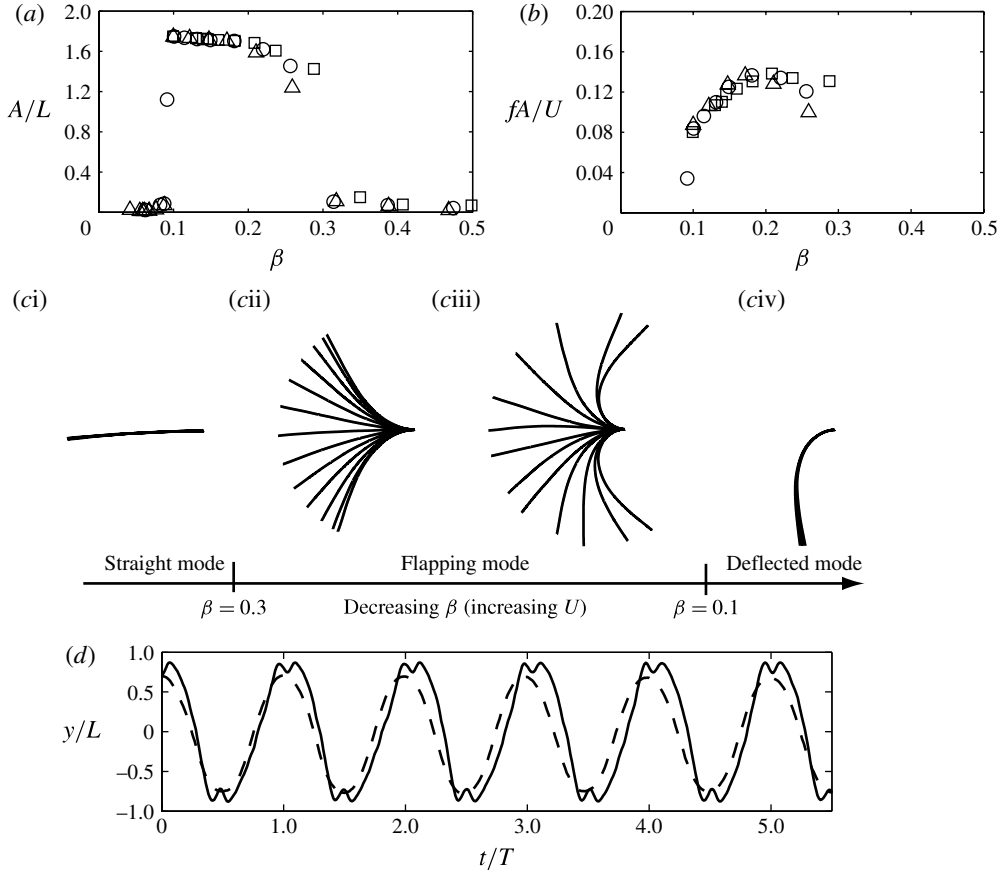
FIGURE 2. (*a*) Peak-to-peak amplitude A/L of the tip and (*b*) Strouhal number fA/U as a function of bending stiffness β for mass ratio of $O(1)$. $H/L = 1.3$ ($\square$); $H/L = 1.1$ ($\bigcirc$); $H/L = 1.0$ ($\triangle$). In (*b*), only the flapping mode with a constant flapping frequency was considered. In the straight and deflected modes, the deflection was not periodic. (*c*) Superimposed sheets at four bending stiffness values: (i) $\beta = 0.58$ ($U = 2.8$ m s^{-1}); (ii) $\beta = 0.26$ ($U = 4.2$ m s^{-1}); (iii) $\beta = 0.10$ ($U = 6.7$ m s^{-1}); (iv) $\beta = 0.06$ ($U = 8.5$ m s^{-1}). $\mu = 2.9$ and $H/L = 1.1$. Gravity is into the paper. See supplementary movies (available at http://dx.doi.org/10.1017/jfm.2013.555) for (i–iv). (*d*) Time history of the *y*-coordinate of the tip $y(s = L)/L$; $\beta = 0.26$ (dashed) and $\beta = 0.10$ (solid). T is a flapping period.

clamped edge does not make much difference compared to the leading edge of the typical flag, flapping of the typical flag type will be likely to occur.

3.2. *Bistability, mode shape, and mass-ratio effect*

Subcritical bifurcation and bistable states are found in the inverted flag (figure 3*a*). Bistable states exist in both straight–flapping mode transition and flapping–deflected mode transition. For increasing non-dimensional free-stream velocity $U^* = \sqrt{1/\beta} = U\sqrt{\rho_f L^3/B}$, the critical velocities U_c^* are 2.1 in the straight–flapping mode bifurcation and 3.4 in the flapping–deflected mode bifurcation for the sheet of $\mu = 2.9$ and $H/L = 1.1$. Then, when U^* decreases for the deflected mode, the sheet tends to maintain its deformed shape and eventually has a slightly lower U_c^* ($=3.3$) than U_c^*
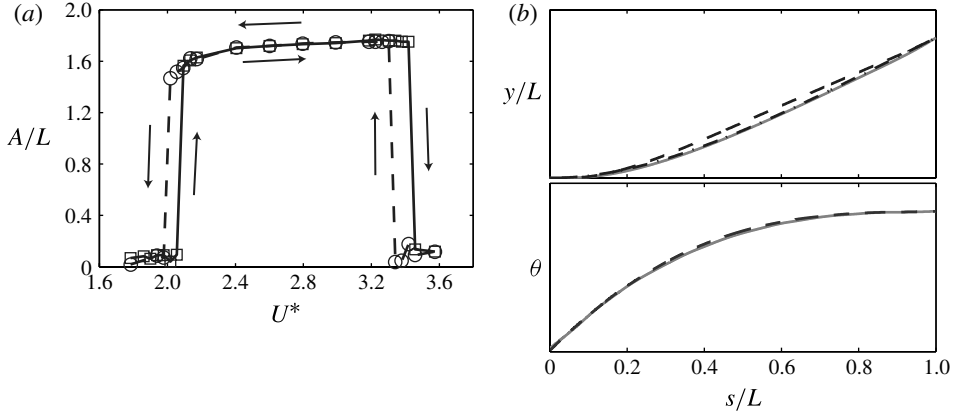
FIGURE 3. (*a*) Hysteresis of amplitude A/L in mode transition: increasing free-stream velocity (solid) and decreasing free-stream velocity (dashed). U^* is non-dimensional free-stream velocity ($= \sqrt{1/\beta}$). (*b*) First-mode shapes of y/L and θ obtained by proper orthogonal decomposition: $\beta = 0.26$ (solid) and $\beta = 0.10$ (dashed), and fundamental mode shape of the linearized Euler–Bernoulli beam (dashed-dot). θ is the angle between the sheet and the $-x$-axis (see figure 1). In both (*a*) and (*b*) $\mu = 2.9$ and $H/L = 1.1$.

for increasing velocity. From the flapping to the straight mode, the initial condition of periodic flapping causes $U_c^*(= 2.0)$ to be also lower than U_c^* for increasing velocity. The U^* widths of the two hysteresis loops are 0.1, and the corresponding dimensional wind velocity ranges in the hysteresis loops are ~ 0.3 m s^{-1}. In spite of the small width of the bistable region, the hysteresis was exhibited consistently in both transitions for every test. In order to check the sensitivity of the hysteresis to the initial alignment of the sheet, the initial angle between the $-x$-axis and the line connecting the tip and the clamped edge was varied. When the initial angle is within $1.5°$, the hysteresis loop still exists. However, for a higher angle, the flapping amplitude A/L tends to increase gradually near the bifurcation, and the hysteresis loop eventually disappears.

Mode shapes of the flapping sheet are obtained by proper orthogonal decomposition (POD) with the time series of the flag position data (Berkooz, Holmes & Lumley 1993). The y-coordinate of the sheet is decomposed with orthogonal modes $\phi_k(s)$ as $y(s, t) = \sum a_k(t)\phi_k(s)$ in the curvilinear coordinate s and time t. The first POD mode $\phi_1(s)$ with the largest eigenvalue is dominant, at which the amplitude of the sheet increases monotonically from the root to the tip (figure 3*b*). The r.m.s. error of the y-coordinate approximated only by the first mode was within 1.5 % of the sheet length over a cycle; the error increases generally as the sheet undergoes large deformation such as for $\beta = 0.1$. For $\beta = 0.26$ with relatively low peak-to-peak amplitude (figure 2*c* ii), the POD mode is similar to the fundamental mode of the linearized Euler–Bernoulli beam equation, $\rho_s h \partial_t^2 y + B \partial_x^4 y = 0$, with free-leading-edge and clamped-trailing-edge boundary conditions. When the amplitude saturates with decreasing β, the POD mode deviates from the fundamental mode, and the mode shape becomes more flattened. The dominance of the first POD mode in the decoupling of spatial and temporal components of $y(s, t)$ clearly shows that the oscillation of the sheet is in a stationary wave form instead of a travelling wave observed in the typical flag (Zhang *et al.* 2000; Michelin *et al.* 2008).
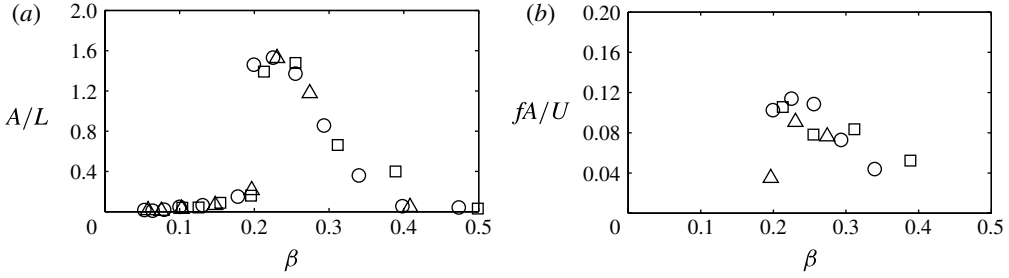
FIGURE 4. (*a*) Peak-to-peak amplitude A/L of the tip and (*b*) Strouhal number $f A/U$ as a function of bending stiffness β for mass ratio of $O(10^{-3})$. $H/L = 2.0$ ($\square$); $H/L = 1.6$ ($\bigcirc$); $H/L = 1.3$ ($\triangle$). In (*b*), only the flapping mode was considered.

The first POD mode of the orientation angle θ, the angle between the sheet and the $-x$-axis at a given s/L (see figure 1), is also presented in figure 3(*b*). θ increases linearly from the clamped trailing edge, but the slope of θ, curvature, reduces gradually along s and reaches zero at the tip. In contrast to the mode shape of y, the mode shapes of θ are almost identical in the flapping mode regardless of bending stiffness β.

For a low mass ratio of $O(10^{-3})$, the sheet can also flap with $A/L > 0.2$ in the range of $0.2 < \beta < 0.4$ (figure 4), which is similar to the flapping range of the high mass ratio (figure 2). However, due to high fluid density and resultant high added-mass effects, the oscillation of $A/L > 1$ occurs in a smaller range of β, $0.2 < \beta < 0.25$. In many cases of the flapping mode, the sheet does not cross the $y = 0$ line after rebounding, but continues to bend and rebound on one y-side only; both maximum and minimum y have the same sign. For this reason, both A/L and $f A/U$ are decreased compared to those of high mass ratio.

The periodic flapping for the low mass ratio is one of the interesting features of the inverted flag. In the typical flag, the critical bending stiffness is nearly linear with μ for $\mu < 1$, and less than 10^{-4} at $\mu = 10^{-3}$ (Alben & Shelley 2008). However, for the inverted flag, the bending stiffness range of the flapping mode is not significantly changed when the mass ratio varies between $O(1)$ and $O(10^{-3})$, but only dynamical behaviours such as amplitude and flapping frequency are affected. In that the inertia effects of the sheet and the surrounding fluid are negligible, static divergence instability rather than flutter instability should be responsible for the unstable motion of the straight sheet (Païdoussis, Price & de Langre 2010). As the lift force exceeds the restoring bending force for decreasing β, the straight sheet starts to bend on one side by buckling, and unsteady flows eventually induce limit-cycle flapping as a post-divergence behaviour.

3.3. *Unsteady force and strain energy*

Once the sheet starts to deflect with high amplitude, the drag exerted on the sheet becomes a major source for bending. Here we examine the dependence of the aerodynamic drag and elastic strain energy on the dynamical modes. Only the cases of high mass ratio $O(1)$ will be considered. Drag coefficient C_D and non-dimensional
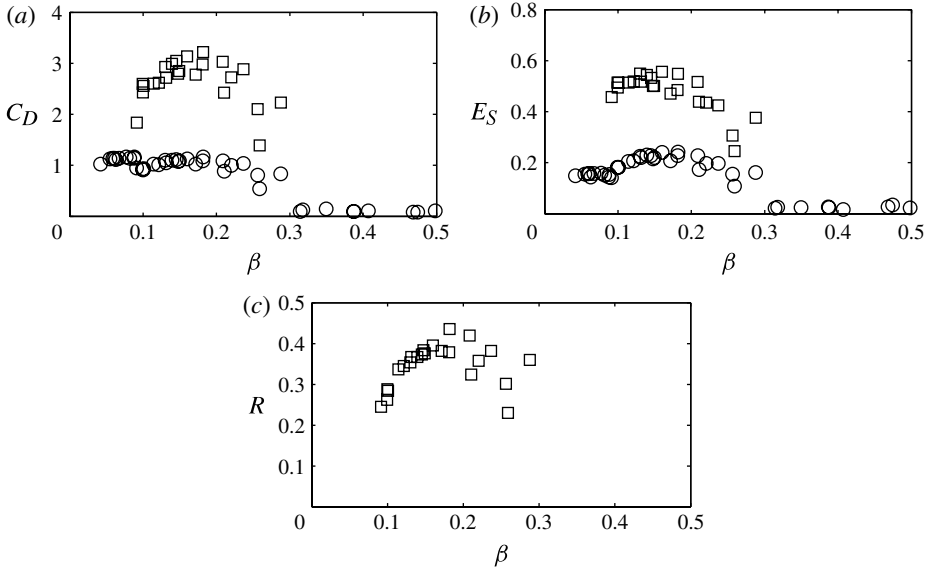
FIGURE 5. (*a*) Drag coefficient C_D and (*b*) elastic strain energy E_S for mass ratio of $O(1)$. Mean C_D and E_S (○); maximum C_D and E_S (□). Maximum C_D and E_S are presented only for the flapping mode. (*c*) Conversion ratio of fluid kinetic energy to strain energy during a bending phase in the flapping mode.

elastic strain energy E_S are defined as follows:

$$C_D(t) = \frac{D(t)}{\frac{1}{2}\rho_f U^2 HL} \quad \text{and} \quad E_S(t) = \frac{\int_0^L \frac{1}{2}BK(s,t)^2 \, \mathrm{d}s}{\rho_f U^2 L^2} = \int_0^1 \frac{1}{2}\beta\kappa(s,t)^2 \, \mathrm{d}(s/L), \quad (3.1)$$

where $K(s,t)$ is a dimensional curvature at a given curvilinear coordinate s and $\kappa = KL$.

Since fA/U is 0.1–0.2 in the flapping mode, unsteady transient force should not be neglected, especially when the sheet has a high angle of attack against the free stream. Thus, the maximum C_D of the flapping mode, which occurs when the tip reaches max $|y|$, is two to three times higher than the mean C_D of the deflected mode (figure 5*a*). Furthermore, although the sheet bends and relaxes repeatedly, the mean C_D of a cycle in the flapping mode is comparable to that of the deflected mode.

The curvature κ of the clamped trailing edge at a maximally deformed phase increases from 4 up to 7–8 as β decreases from 0.3 to 0.1 in the flapping mode. Meanwhile, κ of the trailing edge is between 5 and 8 in the deflected mode. Because of high curvature compared to the deflected mode, the maximum E_S of the flapping mode (≈ 0.40–0.60) is much larger than the mean E_S of the deflected mode (≈ 0.15) (figure 5*b*). As demonstrated in figure 2(*c* iii,iv), despite lower wind velocity, an elastic sheet in the flapping mode can bend downstream more and have higher dimensional strain energy than a sheet in the deflected mode. Moreover, the flapping mode generates a mean E_S higher than that of the deflected mode.

The total kinetic energy of the incoming flow passing through the maximum frontal area during a bending phase is $\hat{E}_K^d = \rho_f U^3 |\hat{y}| H\hat{T}/2$; $|\hat{y}|H$ is the maximum frontal area of the sheet during bending to either positive or negative y-side; $\hat{T}$ is the time from
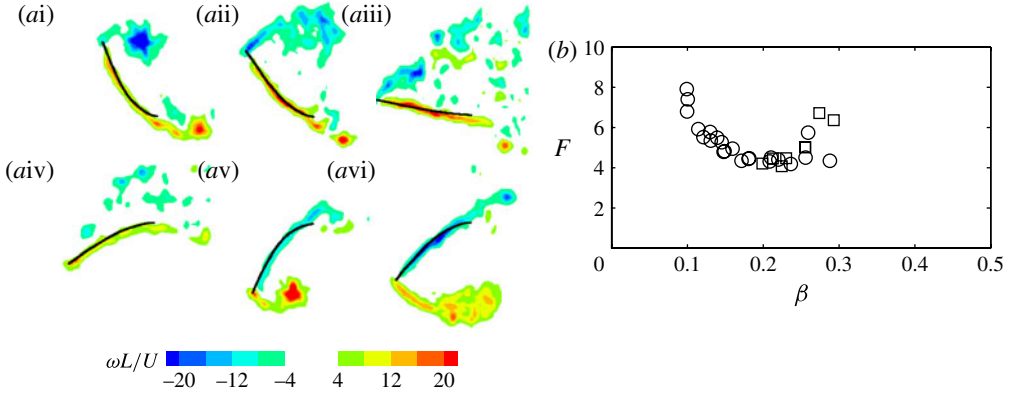
FIGURE 6. (*a*) Sequential vortex formation process in water for low mass ratio of $O(10^{-3})$, vorticity contours ($\beta = 0.19$, $\mu = 0.006$). The sheet (solid line) is at maximum bending in (i) and (v). (*b*) Formation number of the flapping mode. Mass ratio $O(1)$ ($\bigcirc$); mass ratio $O(10^{-3})$ ($\square$). The formation numbers for both positive and negative *y*-sides are averaged.

when the tip of the sheet crosses the $y = 0$ line to when the sheet is at maximum deformation. From (3.1), the conversion ratio from fluid kinetic energy to strain energy during bending is defined as

$$R = \frac{\hat{E}_S^d}{\hat{E}_K^d} = \frac{\int_0^L \frac{1}{2} B \hat{K}^2 \, \mathrm{d}s}{\frac{1}{2} \rho_f U^3 |\hat{y}| \hat{T}}, \qquad (3.2)$$

where $\hat{E}_S^d$ is the dimensional strain energy at maximum deformation. The conversion ratio R is between 0.2 and 0.4 in the bending phase of the flapping mode, and has a peak value near $\beta = 0.17$–0.20 (figure 5*c*). Here R indicates how much elastic strain energy can be stored from fluid kinetic energy flux for the possible energy transfer to other dissipative energy forms. In fact, the strain energy of this elastic sheet is conservative, and no dissipative energy can be extracted. In order to predict actual energy harvesting performance, the conversion of the strain energy to other types of usable energy and its effect on flapping dynamics in both bending and rebounding phases should be investigated, which is beyond the scope of this paper.

3.4. *Leading-edge vortex formation*

Flow visualization shows the correlation between the development of vortex structures and the flapping dynamics of the sheet (figure 6*a*). After the sheet crosses the $y = 0$ line, a vortex starts to form at the leading edge. The leading-edge vortex continues to grow as the sheet bends, and separates from the leading edge and moves downstream as the sheet rebounds. The formation and shedding of the vortex near the leading edge is analogous to the dynamic stall phenomenon of a pitching aerofoil (McCroskey 1981). When the sheet crosses the $y = 0$ line in the opposite direction, a vortex of an opposite sign starts to develop. As a result, alternately signed leading-edge vortices are shed periodically into the wake in response to the flapping frequency of the sheet. Even though visualization in the wind tunnel was not performed in this study, it is reasonable to infer that the flapping of the sheet and the shedding of the leading-edge vortices will be also synchronized for high mass ratio.

The elastic strain energy during the bending process also correlates with the evolution of the leading-edge vortex. The fully developed vortex starts to shed from the leading edge when the sheet starts to rebound from the phase of maximum strain energy. From this observation, we can depict how optimal leading-edge vortex formation is related to the magnitude of strain energy conversion. For this purpose, the concept of formation number is employed. The formation number was first suggested by Gharib, Rambod & Shariff (1998) as a non-dimensional parameter for the time scale of optimal vortex ring formation and successfully applied to biological models (Dabiri & Gharib 2005). Based on Krueger, Dabiri & Gharib (2003), Dabiri & Gharib (2005) and Milano & Gharib (2005), we propose formation number F defined as

$$F = \int_{t_i}^{t_f} \frac{U + u_x(t)}{|\tilde{y}|} \, dt; \qquad (3.3)$$

$t = t_i$ is when the tip crosses the $y = 0$ line, $t = t_f$ is when the sheet is at maximum deformation, and $|\tilde{y}|$ is the y-coordinate magnitude of the tip at $t = t_f$; $u_x(t)$ is the x-directional velocity of the tip. The growth rate of the vortex strength is reduced by the downstream motion u_x of the sheet whose magnitude can be up to $0.6U$. Therefore, $u_x(t)$ is included in the definition of F as suggested in Krueger *et al.* (2003).

For both low and high mass ratios, the formation number F of most flapping cases is within a narrow range between 4.0 and 6.0 even though the flapping dynamics are different among various conditions of β and μ (figure 6b). The F curve as a function of β is of a concave shape and has a trough around $\beta = 0.2$. It is found that F is within the 4.0–4.5 range when β is 0.17–0.20 at which the energy conversion ratio is high (figure 5c). This number is close to the formation number for efficient performance of powered systems such as jet propulsion (Gharib *et al.* 1998; Dabiri & Gharib 2005; Milano & Gharib 2005). Our analysis suggests that the formation number may also be used as a parameter to characterize the relation between optimal vortex formation and efficient storage of strain energy during bending in the self-excited flapping system.

4. Concluding remarks

The flapping dynamics of a self-excited elastic sheet with a free leading edge and a clamped trailing edge were investigated in an effort to better understand the dynamics of unstable structures for potential application to energy harvesting. Instead of maintaining a deflected shape at equilibrium, the inverted flag can flap with large amplitude and store large strain energy because of the unsteady drag force. This flapping mode and the periodic energy conversion to strain energy are limited to a narrow range of the non-dimensional bending stiffness. Interestingly, the inverted flag can flap in a similar range of bending stiffness for the mass ratios of $O(1)$ and $O(10^{-3})$, which implies that the mass ratio is not an important factor in its instability mechanism. It is also demonstrated that the flapping dynamics are closely related to periodic formation and shedding of leading-edge vortices.

Even though some dynamical properties have been examined in this study, the role of the leading-edge vortex on the bifurcation between the stable straight mode and the flapping mode and the mechanism to induce sudden transition from the flapping mode to the quasi-steady deflected mode remain unanswered. These problems will be addressed in the future with rigorous modelling of unsteady force and leading-edge vortex evolution.

Acknowledgement

Supplementary movies

Supplementary movies are available at http://dx.doi.org/10.1017/jfm.2013.555.

References

AKAYDIN, H. D., ELVIN, N. & ANDREOPOULOS, Y. 2010 Wake of a cylinder: a paradigm for energy harvesting with piezoelectric materials. *Exp. Fluids* **49**, 291–304.

ALBEN, S. & SHELLEY, M. J. 2008 Flapping states of a flag in an inviscid fluid: bistability and the transition to chaos. *Phys. Rev. Lett.* **100**, 074301.

ALLEN, J. J. & SMITS, A. J. 2001 Energy harvesting eel. *J. Fluids Struct.* **15**, 629–640.

ARGENTINA, M. & MAHADEVAN, L. 2005 Fluid-flow-induced flutter of a flag. *Proc. Natl Acad. Sci.* **102**, 1829–1834.

BERKOOZ, G., HOLMES, P. & LUMLEY, J. L. 1993 The proper orthogonal decomposition in the analysis of turbulent flows. *Annu. Rev. Fluid Mech.* **25**, 539–575.

BUCHAK, P., ELOY, C. & REIS, P. M. 2010 The clapping book: wind-driven oscillations in a stack of elastic sheets. *Phys. Rev. Lett.* **105**, 194301.

CHANG, Y. B. & MORETTI, P. M. 2002 Flow-induced vibration of free edges of thin films. *J. Fluids Struct.* **16**, 989–1008.

CONNELL, B. S. H. & YUE, D. K. P. 2007 Flapping dynamics of a flag in a uniform stream. *J. Fluid Mech.* **581**, 33–68.

DABIRI, J. O. & GHARIB, M. 2005 The role of optimal vortex formation in biological fluid transport. *Proc. R. Soc. Lond.* B **272**, 1557–1560.

ELOY, C., LAGRANGE, R., SOUILLIEZ, C. & SCHOUVEILER, L. 2008 Aeroelastic instability of cantilevered flexible plates in uniform flow. *J. Fluid Mech.* **611**, 97–106.

GHARIB, M., RAMBOD, E. & SHARIFF, K. 1998 A universal time scale for vortex ring formation. *J. Fluid Mech.* **360**, 121–140.

GUO, C. Q. & PAÏDOUSSIS, M. P. 2000 Stability of rectangular plates with free side-edges in two-dimensional inviscid channel flow. *J. Appl. Mech.* **67**, 171–176.

HUANG, L. 1995 Flutter of cantilevered plates in axial-flow. *J. Fluids Struct.* **9**, 127–147.

JOHNSON, E. & JACOB, J. 2009 Development and testing of a gust and shear wind tunnel for NAVs and MAVs. In *47th AIAA Aerospace Sciences Meeting, Orlando, Florida*.

KRUEGER, P. S., DABIRI, J. O. & GHARIB, M. 2003 Vortex ring pinchoff in the presence of simultaneously initiated uniform background co-flow. *Phys. Fluids* **15**, L49–L52.

LI, S. G., YUAN, J. P. & LIPSON, H. 2011 Ambient wind energy harvesting using cross-flow fluttering. *J. Appl. Phys.* **109**, 026104.

MCCROSKEY, W. J. 1981 The phenomenon of dynamic stall. *NASA Tech. Rep.* 81264.

MICHELIN, S. & DOARÉ, O. 2013 Energy harvesting efficiency of piezoelectric flags in axial flows. *J. Fluid Mech.* **714**, 489–504.

MICHELIN, S., SMITH, S. G. L. & GLOVER, B. J. 2008 Vortex shedding model of a flapping flag. *J. Fluid Mech.* **617**, 1–10.

MILANO, M. & GHARIB, M. 2005 Uncovering the physics of flapping flat plates with artificial evolution. *J. Fluid Mech.* **534**, 403–409.

PAÏDOUSSIS, M. P., PRICE, S. J. & DE LANGRE, E. 2010 *Fluid-Structure Interactions: Cross-Flow-Induced Instabilities*. Cambridge University Press.

RISTROPH, L. & ZHANG, J. 2008 Anomalous hydrodynamic drafting of interacting flapping flags. *Phys. Rev. Lett.* **101**, 194502.

SHAO, C. P., CHEN, Y. J. & LIN, J. Z. 2012 Wind induced deformation and vibration of a platanus acerifolia leaf. *Acta Mechanica Sini* **28**, 583–594.

SHIELS, D., LEONARD, A. & ROSHKO, A. 2001 Flow-induced vibration of a circular cylinder at limiting structural parameters. *J. Fluids Struct.* **15**, 3–21.

TANG, D. M., YAMAMOTO, H. & DOWELL, E. H. 2003 Flutter and limit cycle oscillations of two-dimensional panels in three-dimensional axial flow. *J. Fluids Struct.* **17**, 225–242.

TAYLOR, G. W., BURNS, J. R., KAMMANN, S. M., POWERS, W. B. & WELSH, T. R. 2001 The energy harvesting eel: a small subsurface ocean/river power generator. *IEEE J. Ocean. Engng* **26**, 539–547.

WATANABE, Y., SUZUKI, S., SUGIHARA, M. & SUEOKA, Y. 2002 An experimental study of paper flutter. *J. Fluids Struct.* **16**, 529–542.

ZHANG, J., CHILDRESS, S., LIBCHABER, A. & SHELLEY, M. 2000 Flexible filaments in a flowing soap film as a model for one-dimensional flags in a two-dimensional wind. *Nature* **408**, 835–839.